Acta Geophysica (2023) 71:783–794
https://doi.org/10.1007/s11600-022-00977-3

RESEARCH ARTICLE - APPLIED GEOPHYSICS

Crustal electrical structure across the Tangra-Yumco tectonic belt revealed by magnetotelluric data: new insights on the east–west extension mechanism of the Tibetan plateau

Ning Chen[1,2] · Xuben Wang[1] · Changsheng Shao[3] · Jun Zou[2] · Zhengwei Xu[1] · Dewei Li[1] · Xiangpeng Wang[1]

Received: 18 July 2022 / Accepted: 11 November 2022 / Published online: 27 November 2022

Abstract
Geologic evolution of the Tibetan plateau is characterized by crustal extension and horizontal movement in the post-collision stage, during which, approximate north–south (N–S) trending tectonic belts typically represented by Tangra-Yumco rift are developed. The Tangra-Yumco tectonic belt is an ideal object to investigate the deep structure and mechanism of the crustal extension. The magnetotelluric (MT) method is effective in probing crustal structures, especially for high-conductivity bodies. A MT profile of east–west direction with dense stations has been carried out across the Tangra-Yumco tectonic belt. Resistivity models independently derived from two-dimensional and three-dimensional inversions provided more detailed geophysical constraints on the mechanism of crustal extension and deformation. A significant conductor with estimated melt fraction as 3.0–7.5% in mid-lower crust was revealed under the N–S tectonic belt, where the asthenospheric upwelling through the slab-tearing window might have induced partial melting of the lithospheric mantle and lower crust. Combined with previous studies, the upward migration of hot mantle materials and the expansion of the lower crust should be the primary mechanism driving east–west (E–W) extension of the brittle upper crust with high resistivity above the depth of 30 km. According to lateral electrical discontinuity in the upper crust, we inferred that there might exist three normal faults with the reference of topography and the trend of extension of the existing faults. The expansion and deformation of the conductor might have pulled the brittle upper crust and cause significant E–W extension, leading to the formation of the approximate N–S trending rift and normal faults.

Keywords Electrical structure · Magnetotelluric · Extension · Tibetan plateau · Slab tearing

Introduction

Since the initial collision of India with Asia at about 60 Ma, the Tibetan plateau has experienced complex geologic evolution, including significant crustal shortening, large-scale tectonic deformation and intense crust-mantle interaction (Yin and Harrison 2000; DeCelles et al. 2014). It is generally accepted that the collision of India with Asia has led to large-scale uplifts of the Tibetan plateau and the rise of the Himalayas on the north edge of the Indian continent (Yin 2006; Kapp and DeCelles 2019). The collision can be generally clarified into three stages: syn-collision (65–41 Ma), late-collision (40–26 Ma), and post-collision (< 25 Ma) (Hou and Cook 2009). The post-collision stage is characterized by intense crustal extension and block horizontal movements, which developed a number of approximate N–S striking normal faults and strike-slip faults along northwest or northeast striking directions (Hou et al. 2021). With the

Edited by Dr. Mario Zarroca Hernández (ASSOCIATE EDITOR) / Prof. Gabriela Fernández Viejo (CO-EDITOR-IN-CHIEF).

✉ Xuben Wang
wxb@cdut.edu.cn

[1] College of Geophysics, Chengdu University of Technology, Chengdu 610059, China

[2] Geophysical Exploration Team of Sichuan Bureau of Geology and Mineral Exploration, Chengdu 610072, China

[3] Sichuan Bureau of Geology and Mineral Exploration, Chengdu 610081, China

east–west (E–W) extension of the crust, the approximate north–south (N–S) trending rifts are developed in the central and southern Tibetan plateau.

The mechanism of the crustal extension and deformation is of great significance for understanding the evolution of the Tibetan plateau, of which, the extension and the formation of N–S trending tectonic belts are closely related to the deep structure and the deep deformation. Several formation models have been proposed for the N–S trending tectonic belts of the Tibetan plateau. Some scholars have addressed the formation models controlled by regional stress fields and boundary conditions, such as lateral extrusion model, oroclinal bending model, radial spreading model, and oblique convergence model (Murphy et al. 2009; Styron et al. 2011). Alternatively, the proposed gravitational collapse model links the extension to the uplift of the plateau and the convective removal of lower lithosphere (Molnar et al. 1993). Later on, slab-tearing model has been proposed in previous studies based on the distribution and geologic characteristics of plateau rifts, potassic-ultrapotassic rocks and related deposits (Yin 2000; Hou et al. 2015). From thermodynamic point of view, thermomechanical modeling has indicated that the weak mid-lower crust is essential for the E–W extension of the plateau and the formation of N–S trending rifts (Pang et al. 2018).

Nevertheless, aforementioned models still lacked geophysical evidence to further reveal the mechanism of deep structures and processes, which can provide constraints for further understanding and evaluating various formation mechanisms of the crustal extension. The geophysical prospecting on the deep structures of the plateau revealed low-velocity and high-conductivity bodies in the upper mantle and lower crust, which might be closely related to fluid, partial melting and strength weakening. Under the guide of the magnetotelluric (MT) explorations, widely distributed high-conductivity bodies have been detected in the mid-lower lithosphere of the plateau, where the large-scale conductors should be dominantly caused by partial melting (Unsworth et al. 2005; Wei et al. 2010; Wang et al. 2017). Based on the analysis of high-conductivity bodies under the Yadong-Gulu rift, the formation of the rift is attributed to the possible tearing of Indian lithospheric slab (Wang et al. 2017; Sheng et al. 2021). Coincidentally, seismic tomography has shown that there exist low-velocity anomalies in the upper mantle under rift zones, which were interpreted to be mainly associated with the possible slab tearing and asthenospheric upwellings (Liang et al. 2016; Li and Song 2018).

However, the seismic research paid more attention on the general structures in the upper mantle beneath the central and southern Tibetan plateau. Meanwhile, it is worth noting that previous seismic studies were based on data acquired from sparse stations. Similarly, the referable MT data across the Yadong-Gulu rift, as one of the N–S tectonic belts, were recorded with sparse data stations. Therefore, these subsistent data might not be able to comprehensively reveal detailed crustal structures under N–S tectonic belts, which gives rise to the lack of systematic understanding on the crustal extension mechanism.

In this paper, another N–S trending tectonic belt in Tangra-Yumco region was chosen as the primary study area. The magnetotelluric method is effective in probing the crustal structure, especially for high-conductivity bodies. For the purpose of obtaining reliable constraints on crustal deformation and extension mechanism, a MT profile was deployed along the E–W direction with 41 dense stations and average spacing of 2.3 km across the Tangra-Yumco tectonic belt. The high-quality impedance tensor data at the periods of 0.01–2000s were obtained for the study of the crustal electrical structure. Two reliable resistivity models derived from two-dimensional (2-D) and three-dimensional (3-D) inversions can mutually provide geophysical constraints for the deformation and formation mechanism of the N–S tectonic belts, resulting in new insights on the E–W extension mechanism of the Tibetan plateau.

Geological setting

In the south of the study area located in the central Tibetan plateau (Fig. 1), the Lhasa terrane is mainly covered by Carboniferous-Permian sedimentary sequences and Jurassic-Tertiary volcano-sedimentary sequences, and Cretaceous intrusions are developed (Pan et al. 2013). The Qiangtang terrane in the north dominantly exposes Triassic-Cretaceous sedimentary sequences and Triassic-Jurassic intrusive rocks (Chen et al. 2020). Bangong-Nujiang suture zone (BNSZ) is a mélange zone containing ophiolitic rocks.

The approximate north–south trending tectonic belts are mainly composed of rifts and normal faults on the edges of the rifts (Fig. 1). The normal faults on both sides of the Tangra-Yumco rift are inclined toward each other, and the Cenozoic thrust faults in the study area extends mainly along the E–W direction (Pan et al. 2013). The N–S striking normal faults extend intermittently northward through the BNSZ and into the Qiangtang terrane. The ages of the dikes along the N–S trending normal faults range from 18.3 ± 2.7 Ma to 13.3 ± 0.8 Ma (Williams et al. 2001). The eruption and distribution of the potassic-ultrapotassic rocks in central Tibet is closely associated with the N–S faults system, and the ages of the ultrapotassic rocks along the Tangra-Yumco rift range from 23 to 8 Ma (Zhao et al. 2006; Zheng et al. 2016). There are a series of lakes and extensional basins of varying sizes along the N–S trending tectonic belt, which are considered as the products of crustal extension (Kapp et al. 2008).

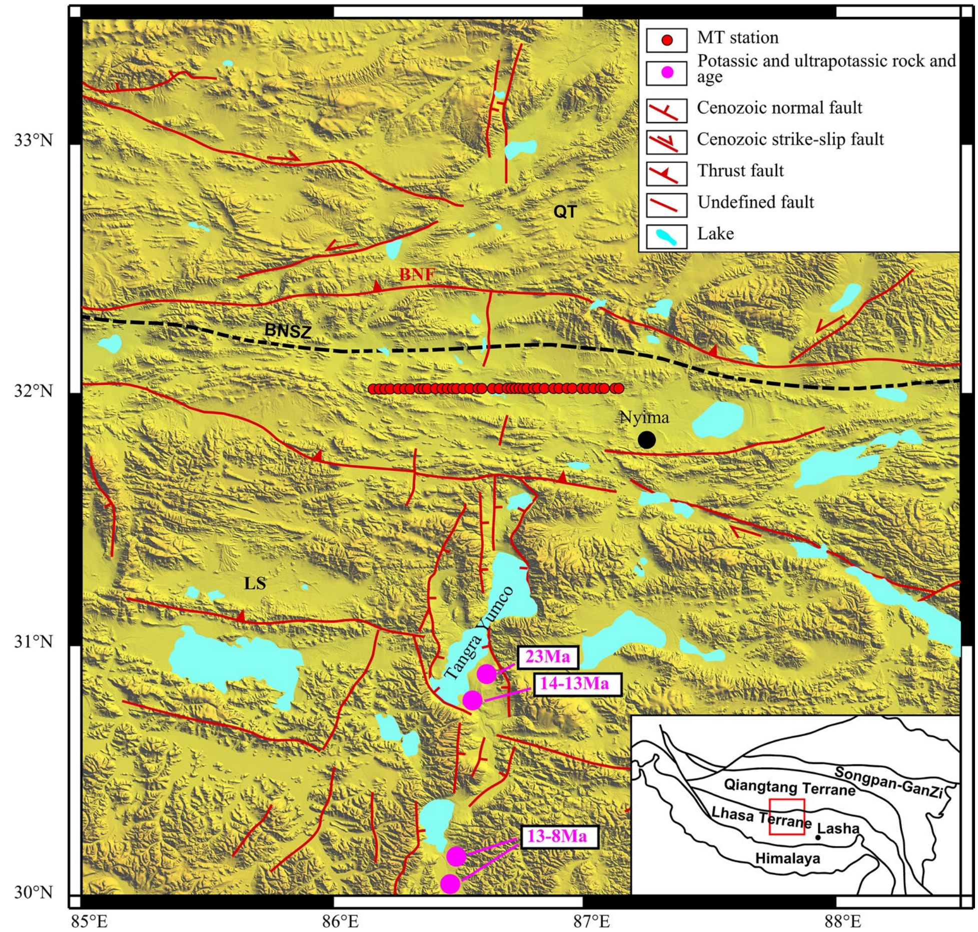

Fig. 1 Map of topographic features, tectonic diagram, and MT stations in Tangra-Yumco region. QT: Qiangtang terrane; LS: Lhasa terrane; BNSZ: Bangong-Nujiang suture zone; BNF: Bangong-Nujiang fault

MT data acquisition, processing and analysis

Data acquisition and processing

The MT profile with dense stations has been carried out across the Tangra-Yumco tectonic belt along the E–W direction (Fig. 1). The profile with a total length of about 92 km includes 41 MT stations with an average spacing of about 2.3 km. MT data were acquired two horizontal electric field components (E_x and E_y) and two horizontal components of magnetic field (H_x and H_y), using MTU-5A instruments with recording time over 20 h. The MT data were processed using the SSMT2000 software of Phoenix Geophysics and the robust estimation algorithm proposed by Egbert (1997), converting the raw data to the high-quality impedance tensor data at periods of 0.01–2000s.

Dimensionality and strike direction

In order to determine which dimension of inversion might be suitable for this case, the phase tensor method (Caldwell et al. 2004), avoiding the influence of local electric field distortion, was conducted to assess the dimensionality of the MT dataset. The phase tensor is defined as three invariants: the maximum phase (Φ_{max}), the minimum phase (Φ_{min}) and the skew angle (β). The results are plotted as ellipses shown in Fig. 2 with the maximum phase as major axis and the minimum phase as minor axis, and the ellipses are colored by corresponding skew angle (β). Especially at the short period of 1 s, most of the skew angles are less than 3°, which denotes that two-dimensionality might be dominated (Booker 2014), indicating shallow quasi 2-D electrical structure of the study area. Nevertheless, a few large skew angles (> 5°) were identified at the long periods of 100 s and 1000 s, which may indicate the emergence of 3-D resistivity structures in the deep depth. Therefore, in this paper, 2-D and 3-D inversion scheme might be independently carried out for comprehensively interpretation on the shallow small-scale and deep complex structures.

For the stage of the 2-D inversion, it is of importance to determine the strike direction to calibrate coordination system, where the MT data can be decomposed into two independent modes, i.e., transverse electric (TE) mode and the transverse magnetic (TM) mode. The strike analysis results of the phase tensor method were plotted as rose diagrams of different period range shown in the Fig. 2,

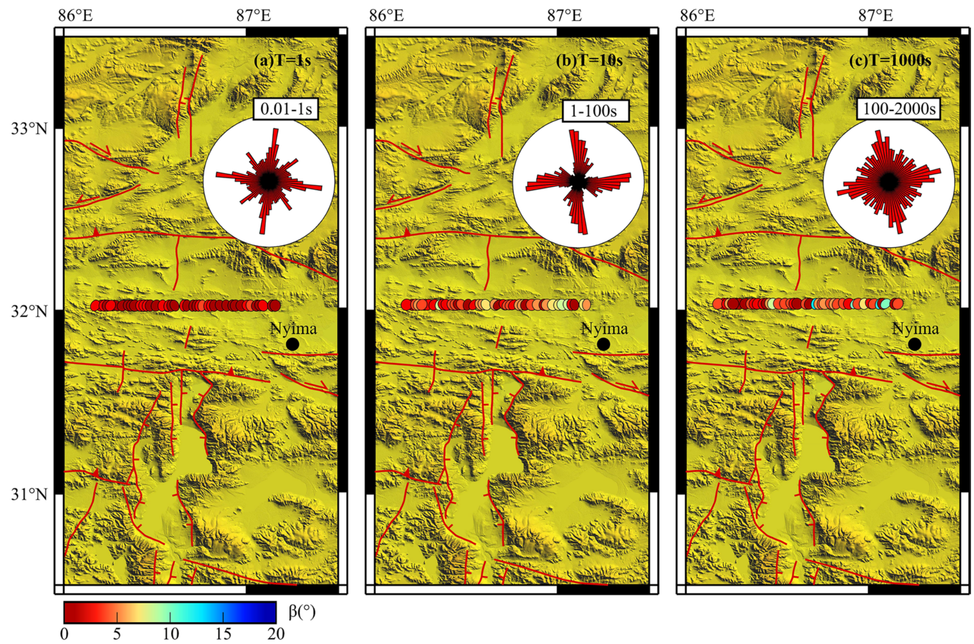

Fig. 2 Phase tensor ellipses and rose diagrams. The ellipses are colored by skew angle β at three periods (1 s, 10 s, 1000 s), and the rose diagrams represent strike angles with different period ranges of 0.01–1 s, 1–100 s and 100–2000s

indicating that the regional strike angle is approximately oriented along N–S or E–W direction. Combined with approximate N–S trending direction of the Tangra-Yumco tectonic belt, the N–S direction was chosen as the regional strike direction for the MT profile.

Data inversion

Two-dimensional inversion

After determining the strike direction, the decomposed electric field of TE mode and the magnetic field of TM mode were inverted to get a 2-D resistivity model with an initial model of 100 Ωm half space, using the nonlinear conjugate gradients (NLCG) algorithm (Rodi and Mackie 2001) in the WinGLink software package. On account of the effect of static shifts, downweighting the apparent resistivity was carried out in the 2-D inversion (Ye et al. 2019). Since the TE mode is more effective to the vertical electrical structure and the TM mode is more sensitive to the horizontal electrical variations (Becken et al. 2008), we comprehensively integrated both two modes into the inversion. The error floors of the TM mode were set as 10% and 5% for the apparent resistivity and phase, respectively. Considering the TE mode data are more easily affected by 3-D effects than the TM mode data, the error floors for the apparent resistivity and phase of the TE mode were set as 40% and 20%. After analyzing the L-curve shown in Fig. 3, the regularization factor τ was set to 5 (Farquharson and Oldenburg 2004). The ratio between the horizontal and vertical smoothing factors was set to 1. After 100 iterations, the root-mean-square (RMS) misfit decreased from 6.332 to 1.117 with the period of 0.01–2000s. Combined with the comparison of pseudosections in Fig. 4, global and site-by-site RMS misfits (Fig. 5a) show the high degree of fitting between calculated model response and measured data. The 2-D recovered resistivity model is shown in Fig. 5c, representing high resistivity of the upper crust and a significant high-conductivity body (C1) in the mid-lower crust.

After obtaining the 2-D resistivity model, it is important to conduct sensitivity tests to confirm whether the model corresponds with the measured data. In this paper, the sensitivity was determined by editing the original 2-D resistivity model and comparing the discrepancy of fitting conditions before and after the modification. As shown Fig. 6, the changes in the low boundary of the original resistivity model led to obvious increases in the global and site-by-site RMS misfit values. The test results show that the measured data are sensitive to the changes of electrical structure.

Three-dimensional inversion

Since the MT dataset showed the three-dimensionality features, 3-D inversions were subsequently conducted using the ModEM software (Egbert and Kelbert 2012; Kelbert et al. 2014). The full impedance elements (Z_{xx}, Z_{xy}, Z_{yy}, Z_{yx}) were inverted with 36 periods ranging from 0.01 to 2000s. The error floor for off-diagonal elements was set to 5% of $|Z_{xy} \times Z_{yx}|^{1/2}$ and 10% for diagonal elements. The model space was discretized with horizontal grid spacing of 1.4 km × 1.4 km in the core area and padded with 12 cells on all edges, where the grid spacing gradually increase with a factor of 1.5. The model area was designed from − 550 to

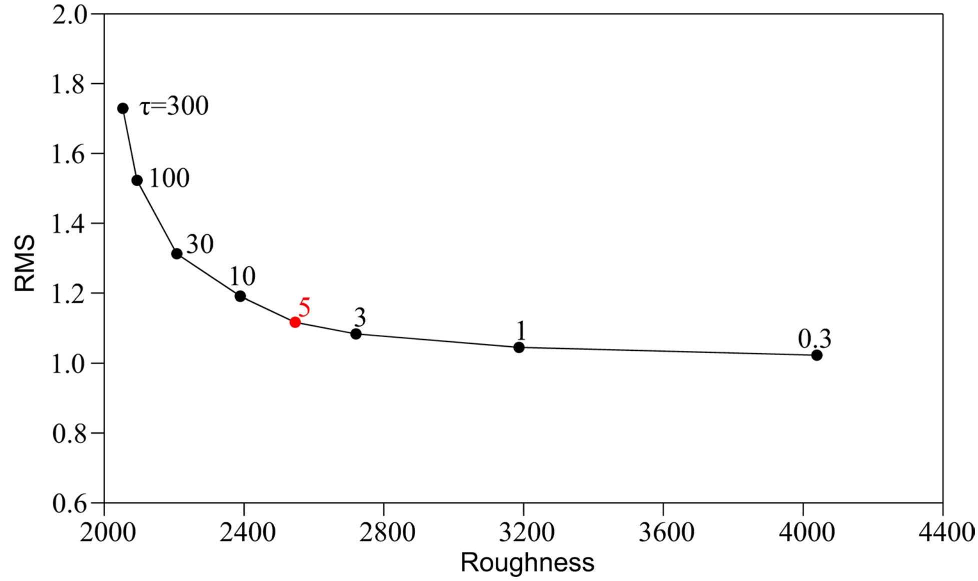

Fig. 3 Illustration of the relationship between RMS and roughness corresponding to different τ values. Regularization τ = 5 (red dot) was chosen at the inflection point in the L-curve

550 km along the *x*-axis and *y*-axis, respectively. In the vertical direction, the thickness of the first layer was set to 50 m and 63 layers were included. Similarity as the horizontal discretization, the thicknesses of the upper 55 vertical layers gradually increased with a factor of 1.1, and the thicknesses of the rest 8 layers below were padded with an increasing factor of 1.5. The total depth of the model was up to 668 km. The 3-D inversion started from an initial model of 100Ωm half space. After 100 iterations, the global RMS misfit decreased from 6.65 to 1.406. Figure 7 shows the fitting behaviors of apparent resistivity and phase at station 16 and 24, respectively, and the RMS misfits of most stations shown in Fig. 8a are less than 2, indicating that the measured data and model responses are well-matched. The 3-D resistivity model is shown in Fig. 8c, one can see that although there are some discrepancies in the shape of abnormal bodies as the 2-D result, the 3-D inversion remains the main features of the electrical structures in the subsurface.

As shown in Fig. 9, changes in the low boundary of the original resistivity model of the 3-D inversion lead to significant increases in the global and site-by-site RMS misfit values. The test results show that the observed data are sensitive to the changes of electrical structure at the bottom as well.

In summary, as shown in Fig. 5c and Fig. 8c, the inversion models provide detailed resistivity structures of the N–S trending tectonic belt in Tangra-Yumco region, revealing the obvious electrical discrepancy between the upper and the mid-lower crust. One can see that the upper crust is characterized by high resistivity, and the mid-lower crust shows the feature of high conductivity. There are two high-resistivity bodies (R1 and R2) identified in the upper crust and a large-scale high-conductivity body (C1) in the mid-lower crust under the N–S trending tectonic belt.

Interpretation and discussion

Origin and analysis of the conductor C1

It is worth noting that the remarkable and uniform feature of both 2-D and 3-D inversion results is the conductor (C1) with a trend of extending to the deep lithosphere in the mid-lower crust and against the bottom of the upper crust (Fig. 5c and Fig. 8c). Previous seismic studies have revealed lateral variations along the N–S trending tectonic belts in southern Tibet by the SKS-wave splitting measurements and the obvious differences in subduction angles of the Indian lithospheric slab by receiver function techniques (Chen et al. 2015; Zhao et al. 2010), which indicate the increases in the subduction angles from west to east and the possible slab tearing. Seismic tomography shows a series of low-velocity anomalies in the upper mantle under the N–S rifts (Liang et al. 2016; Li and Song 2018), which suggest the possible slab tearing and local asthenospheric upwellings. Furthermore, the distribution of the potassic-ultrapotassic rocks along the N–S trending tectonic belts might infer the upwelling of the asthenosphere and partially molten lithospheric mantle (Zhao et al. 2006; Zheng et al. 2016; Guo and Wilson 2019; Hou et al. 2021). Therefore, the conductor C1 recovered from the 2-D and 3-D inversions might be induced by the upward migration of hot mantle materials (Fig. 11).

Previous studies have suggested that partial melting or aqueous fluids are the most likely cause for the large-scale high-conductivity bodies in southern Tibet (Unsworth et al. 2005; Chen et al. 2018). The studies on granulite xenoliths in the north of our study area have inferred the high-temperature state of the lower crust (Hou et al. 2021). There exist high heat flow values around the

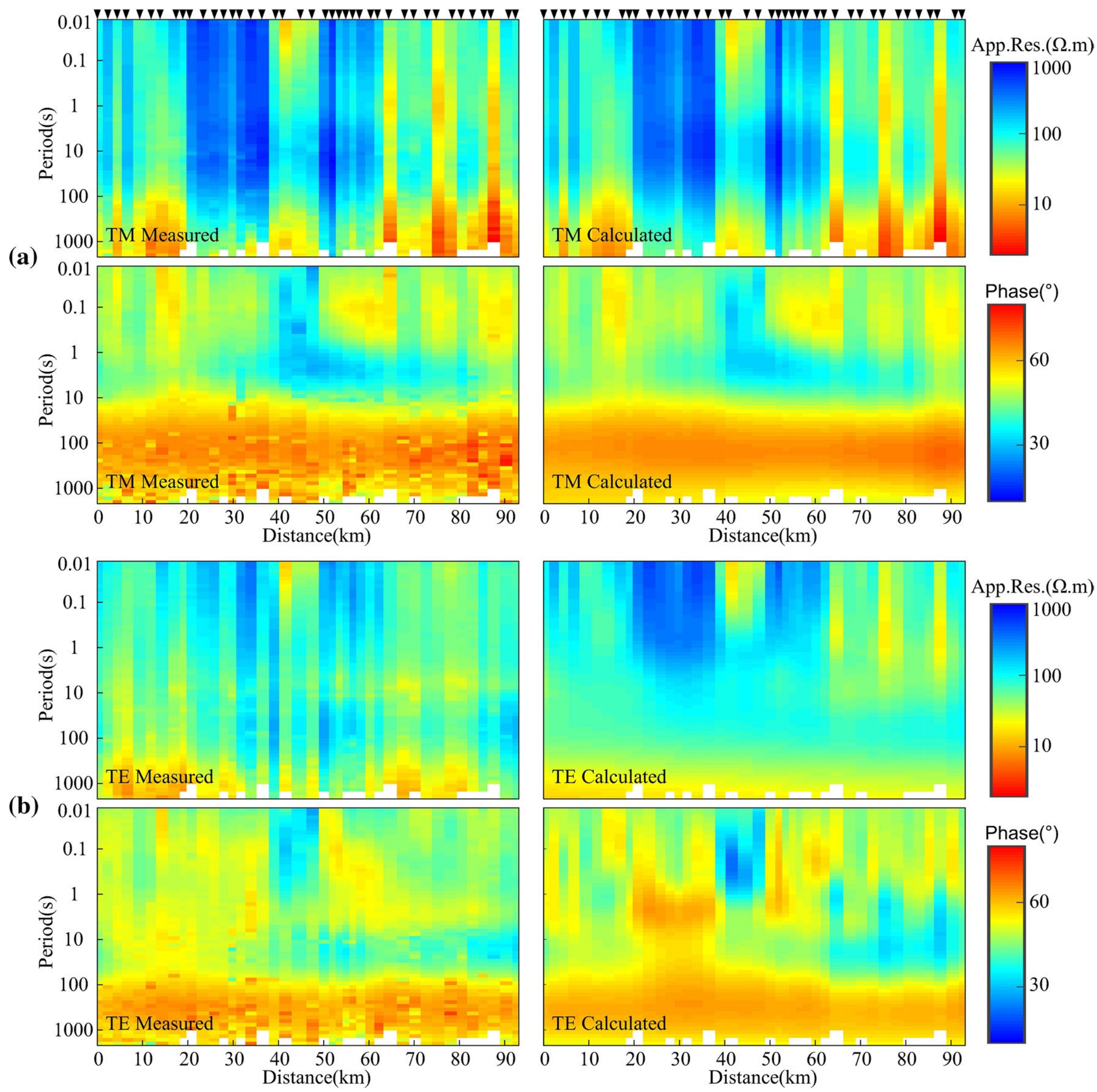

Fig. 4 Pseudosections of measured data and calculated model response. **a** TM mode, **b** TE mode

Yarlung-Zangbo suture zone and N–S rift zones in southern Tibet (Francheteau, et al. 1984; Jiang et al. 2016). Under the high-temperature thermal state, aqueous fluids that can lower the melting point are unlikely to be preserved in the mid-lower crust for long term of geologic timescales. As discussed above, the high-conductivity body (C1) should be dominantly caused by partial melting.

For quantitatively estimating the melt fraction of the conductor C1, we used the modified Archie's law that is suitable in southern Tibet (Rippe and Unsworth, 2010; Bai et al. 2010). The law can be expressed as:

$$\rho_{\text{eff}} = A_{\text{eff}}^{-1}\Phi^{-n}\rho_{\text{m}},$$

where ρ_{eff} represents the bulk resistivity, Φ is the melt fraction, and ρ_{m} is defined as pure melt resistivity. It was suggested to set the coefficients A_{eff} and n as 1.47 and 1.3, respectively (Ten Grotenhuis et al. 2005). The ρ_{m} was assumed to be 0.1–0.3Ωm (Unsworth et al. 2005). For a given thickness, the bulk resistivity is determined by the ratio of conductance to thickness. The bulk resistivity of conductor C1 is about 6 Ωm.

Laboratory experiments showed that 5–7% melt fraction of aplite can reduce its effective viscosity by an order of magnitude (Unsworth et al. 2005; Rosenberg and Handy 2005). As shown in Fig. 10, the melt fraction is about 3.0–7.5%, which reaches the amount required for strain localization in geodynamic models (Beaumont et al 2001). Based on above analysis, the increase in melt

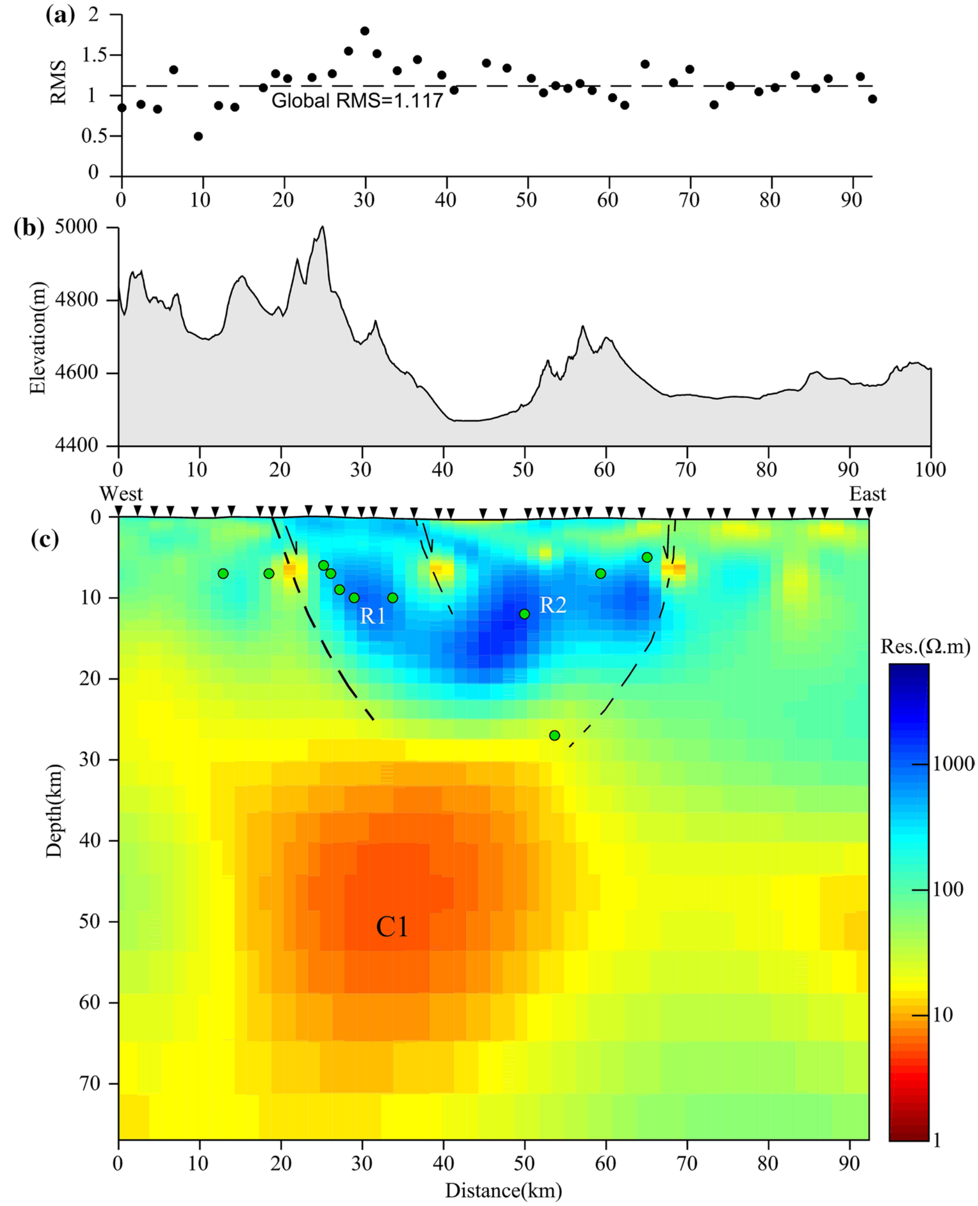

Fig. 5 Two-dimensional inversion resistivity model and tectonic interpretation. **a** Global and site-by-site RMS distribution. **b** Topography along the MT profile. **c** Resistivity model with tectonic interpretation and earthquakes. Black dashed lines are inferred faults, and green dots are the projection of the earthquakes (M > 3) from 1970 to 2022 within the latitude range of 0.5° on both sides of the MT profile. Black triangles above the resistivity model represent MT stations

fraction can significantly reduce the effective viscosity and strength of the crust, and the conductor C1 under the Tangra-Yumco tectonic belt meets the condition for deformation.

Formation mechanism of the N–S tectonic belt

It shows that the apparent discrepancies between the upper and the mid-lower crust can be roughly differentiated at the depth of about 30 km. As shown in Fig. 5c and Fig. 8c, the distribution of the earthquakes collected adjacent to the profile are coincidentally around the edges of the two high-resistivity bodies (R1 and R2) above the differentiated depth. Given that earthquakes usually occur within brittle crust by strain accumulation and brittle deformation, we infer that the area around the differentiated depth might be considered as a transition zone connecting the ductile mid-lower crust with the brittle upper crust.

Under the guide of the aforementioned mechanism of the slab tearing and asthenosphere upwelling (Fig. 11a), the partial melting of the mid-lower crust (conductor C1) under the N–S tectonic belt can significantly reduce its viscosity and strength, which meets the condition for strain localization and deformation. The upward migration of the hot mantle materials could have driven the expansion and deformation of the partially molten crust (conductor C1) (Fig. 11b). In addition, referring with topography and the extending trend of N–S normal faults, we infer three concealed normal faults of the brittle crust throughout three apparent relative low resistivity zones and along the lateral electrical discontinuity

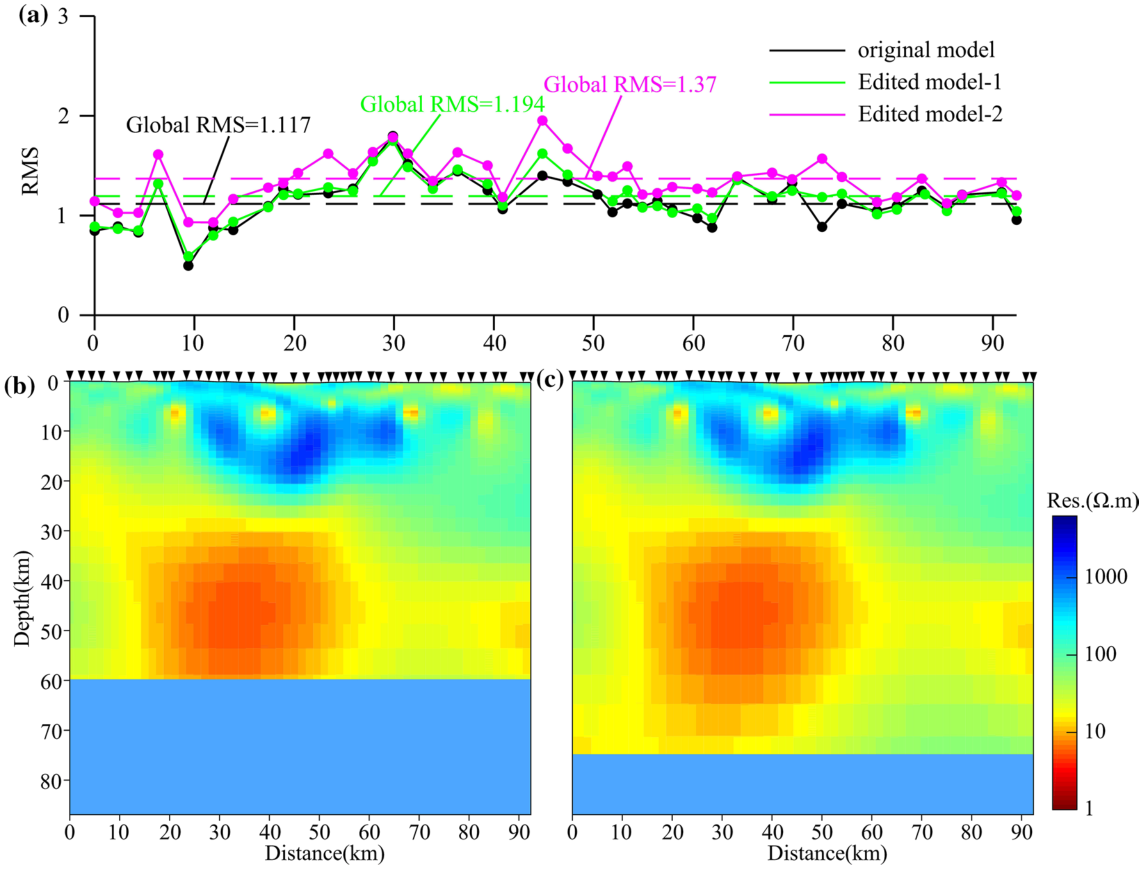

Fig. 6 Illustration of sensitivity tests for 2-D inversion model. **a** Comparison of RMS misfits between 2-D original resistivity model and edited models. **b** The edited model-1 filling with 1000 Ωm below the depth of 60 km. **c** The edited model-2 filling with 1000 Ωm below the depth of 75 km

Fig. 7 Fitting behaviors of apparent resistivity and phase at station 15 and 24, respectively. Symbols of circles and squares represent measured E_x–H_y and E_y–H_x, respectively. Solid lines correspond to model responses of 3-D inversion model

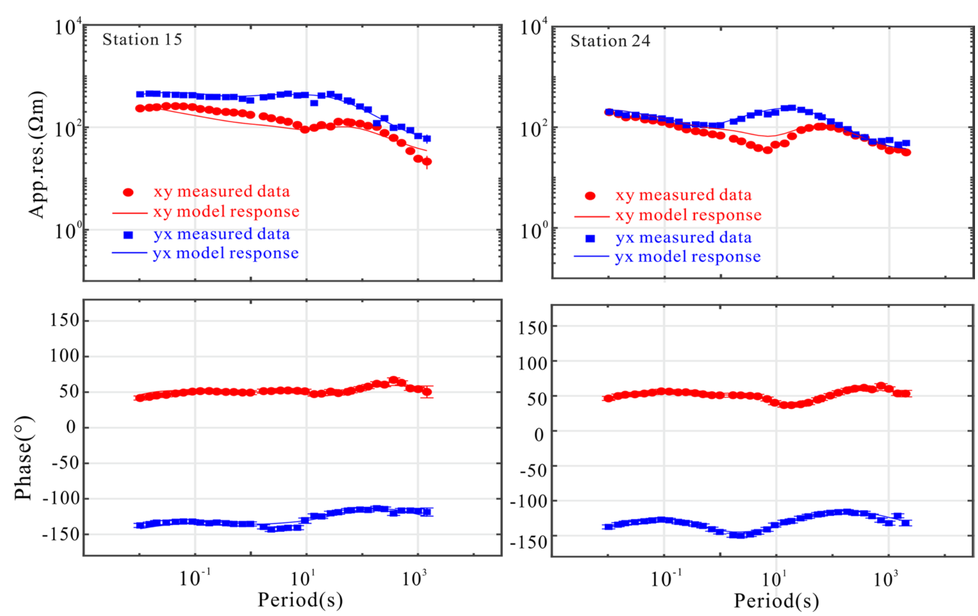

Fig. 8 Three-dimensional inversion resistivity model and tectonic interpretation. **a** Global and site-by-site RMS distribution. **b** Topography along the profile. **c** Resistivity model with tectonic interpretation and earthquakes. Black dashed lines are inferred faults, and the green dots are the projection of the earthquakes (M > 3) from 1970 to 2022 within the latitude range of 0.5° on both sides of the MT profile. Black triangles above the resistivity model represent MT stations

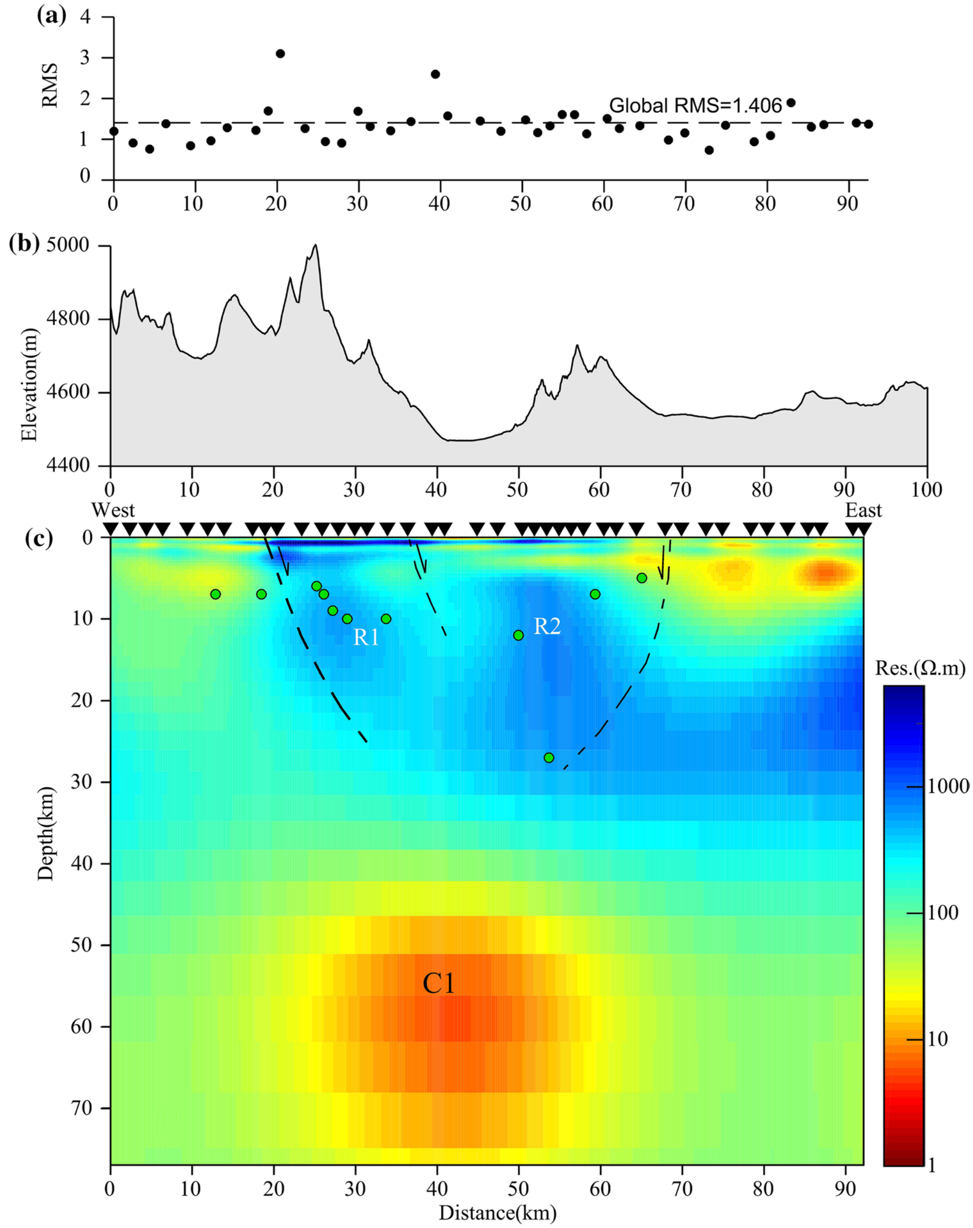

boundaries (Fig. 5 and Fig. 8). Moreover, the thermomechanical modeling results have suggested that the weak mid-lower crust is essential for the E–W extension of the plateau and the formation of N–S rifts (Pang et al. 2018). Therefore, the expansion and deformation of the conductor C1 could have pulled the brittle upper crust and subsequently caused the significant E–W extension, leading to the formation of the approximate N–S trending rift and normal faults. With the upward migration of the hot mantle materials, the magmatism should develop, and the high-resistivity bodies (R1 and R2) are most likely to reflect the presence of intrusive rocks (Fig. 5c and Fig. 8c).

Conclusions

The MT profile across the approximate N–S trending tectonic belt was carried out, and the results from the 2-D and 3-D inversions have provided the detailed resistivity models for the study on the deep structure and formation mechanism of the E–W extension in the Tibetan plateau. The conductor C1 should be caused by partial melting with the estimated melt fraction as 3.0–7.5%, which should lead to the low viscosity and weak strength of the mid-lower crust under the N–S trending tectonic belt. Comprehensively combined with the characteristics of seismic anomalies, tectonic activities and potassic-ultrapotassic magmatism, the conductor C1 is most likely induced by the asthenospheric upwelling through

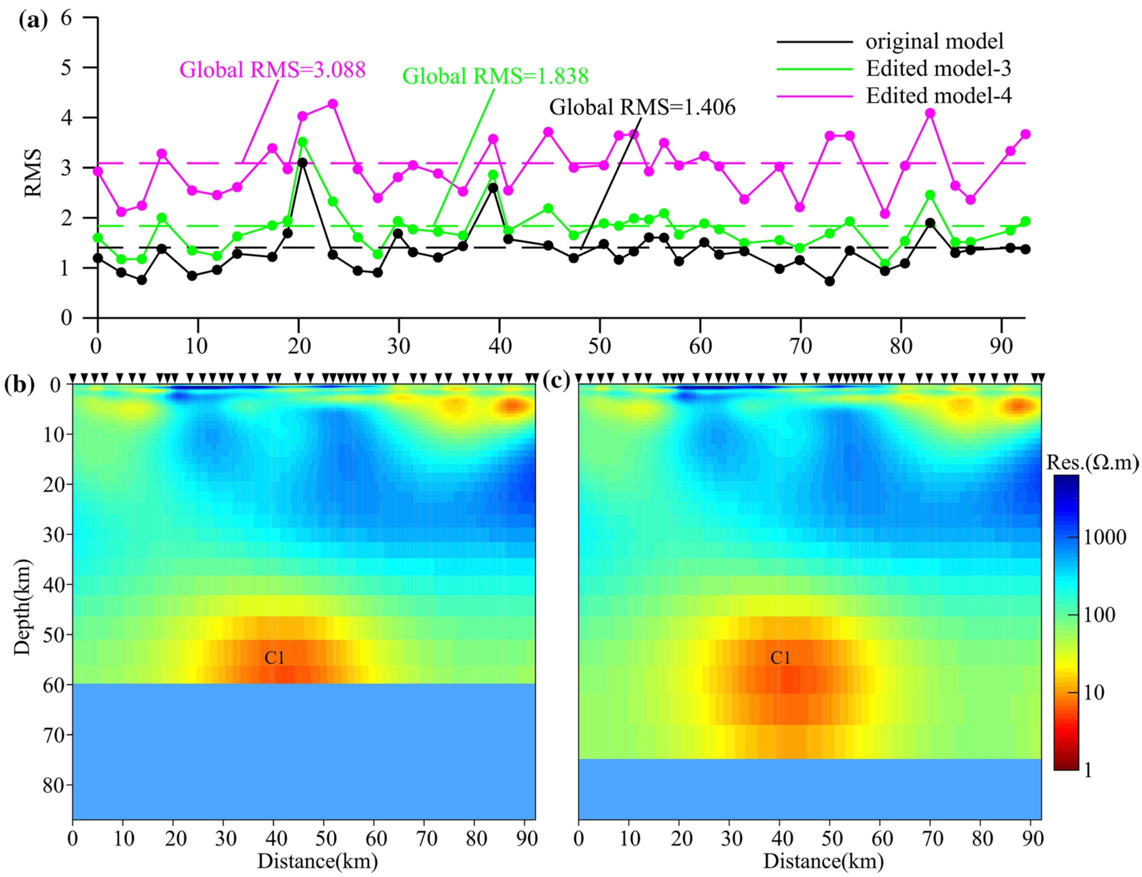

Fig. 9 Illustration of sensitivity tests for 3-D inversion model. **a** Comparison of RMS misfits between 3-D original resistivity model and edited models. **b** The edited model-3 filling with 1000 Ωm below the depth of 60 km. **c** The edited model-4 filling with 1000 Ωm below the depth of 75 km

Fig. 10 Relationship between bulk resistivity and melt fraction. The pure melt resistivity is assumed as 0.1–0.3 Ωm. The bulk resistivity of the high-conductivity body (C1) is about 6 Ωm, and the melt fraction range is shown as the shaded area

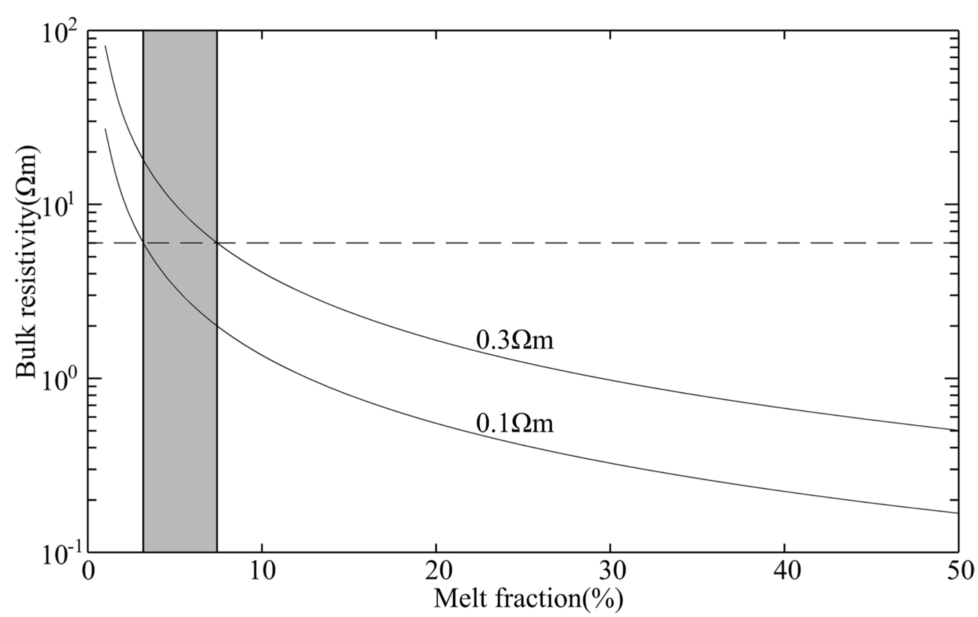

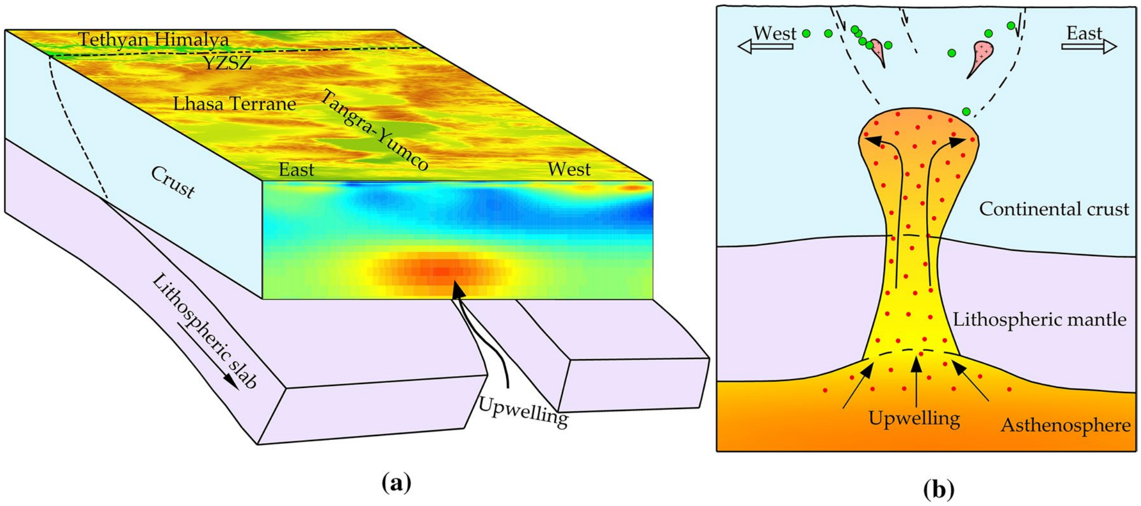

Fig. 11 **a** Slab-tearing model; **b** The mechanism of E–W extension. Slab tearing might induce the upwelling of asthenosphere and partial melting of the Lithospheric mantle and mid-lower crust under the N–S tectonic belt. The upward migration of hot mantle materials could have driven the expansion and deformation of the partially molten crust with low viscosity and strength, which could have pulled the brittle upper crust and cause significant E–W extension, resulting in the formation of approximate N–S trending rift and normal faults

the slab-tearing window and the upward migration of the hot mantle materials, further providing partial evidence for the existing slab-tearing model for the E–W extension of the plateau. The inversion models revealed the brittle upper crust characterized by high resistivity and the ductile mid-lower crust with high conductivity. The upward migration of the hot mantle materials should have driven the expansion and deformation of the conductor C1, which, in subsequent, could have pulled the brittle upper crust, resulting in the E–W extension of the plateau and the formation of N–S trending rift and normal faults.

Acknowledgements This study was funded by National Natural Science Foundation of China (Grant no. 91755215, 41930112). We would like to thank our field crews and students for their hard work in data collection and preparation. We are grateful to Sichuan Bureau of Nuclear Industry and Geology for their assistance in instruments. We also thank Gary Egbert and Anna Kelbert for providing their 3-D MT inversion code ModEM. Special thanks must go to editors and reviewers for their hard work and valuable comments.

Declarations

Conflict of interest All authors declare that they have no conflicts of interest to this work.

References

Bai DH, Unsworth MJ, Meju MA, Ma XB, Teng JW, Kong XR, Sun Y, Sun J, Wang LF, Jiang CS, Zhao CP, Xiao PF, Liu M (2010) Crustal deformation of the eastern Tibetan plateau revealed by magnetotelluric imaging. Nat Geosci 3:358–362. https://doi.org/10.1038/ngeo830

Beaumont C, Jamieson RA, Nguyen MH, Lee B (2001) Himalayan tectonics explained by extrusion of a low-viscosity crustal channel coupled to focused surface denudation. Nature 414:738–742. https://doi.org/10.1038/414738a

Becken M, Ritter O, Burkhardt H (2008) Mode separation of magnetotelluric responses in three-dimensional environments. Geophys J Int 172:67–86. https://doi.org/10.1111/j.1365-246X.2007.03612.x

Booker JR (2014) The magnetotelluric phase tensor: a critical review. Surv Geophys 35:7–40. https://doi.org/10.1007/s10712-013-9234-2

Caldwell TG, Bibby HM, Brown C (2004) The magnetotelluric phase tensor. Geophys J Int 158:457–469. https://doi.org/10.1111/j.1365-246X.2004.02281.x

Chen Y, Li W, Yuan XH, Badal J, Teng JW (2015) Tearing of the Indian lithospheric slab beneath southern Tibet revealed by SKS-wave splitting measurements. Earth Planet Sc Lett 413:13–24. https://doi.org/10.1016/j.epsl.2014.12.041

Chen JY, Gaillard F, Villaros A, Yang XS, Laumonier M, Jolivet L, Unsworth M, Hashim L, Scaillet B, Richard G (2018) Melting conditions in the modern Tibetan crust since the Miocene. Nat Commun 9:3515. https://doi.org/10.1038/s41467-018-05934-7

Chen YF, Ding L, Li ZY, Laskowski AK, Li JX, Baral U, Qasim M, Yue YH (2020) Provenance analysis of Cretaceous peripheral foreland basin in central Tibet: Implications to precise timing on the initial Lhasa-Qiangtang collision. Tectonophysics 775:228311. https://doi.org/10.1016/j.tecto.2019.228311

DeCelles PG, Kapp P, Gehrels GE, Ding L (2014) Paleocene-Eocene foreland basin evolution in the Himalaya of southern Tibet and Nepal: implications for the age of initial India-Asia collision. Tectonics 33:824–849. https://doi.org/10.1002/2014TC003522

Egbert GD (1997) Robust multiple-station magnetotelluric data processing. Geophys J Int 130:475–496. https://doi.org/10.1111/j.1365-246X.1997.tb05663.x

Egbert GD, Kelbert A (2012) Computational recipes for electromagnetic inverse problems. Geophys J Int 189:251–267. https://doi.org/10.1111/j.1365-246X.2011.05347.x

Farquharson CG, Oldenburg DW (2004) A comparison of automatic techniques for estimating the regularization parameter in non-linear inverse problems. Geophys J Int 156:411–425. https://doi.org/10.1111/j.1365-246X.2004.02190.x

Francheteau J, Jaupart C, Shen XJ, Kang WH, Lee DL, Bai JC, Wei HP, Deng HY (1984) High heat flow in southern Tibet. Nature 307:32–36. https://doi.org/10.1038/307032a0
Guo ZF, Wilson M (2019) Late Oligocene–early Miocene transformation of postcollisional magmatism in Tibet. Geology 47:776–780. https://doi.org/10.1130/G46147.1
Hou ZQ, Cook NJ (2009) Metallogenesis of the Tibetan collisional orogen: a review and introduction to the special issue. Ore Geol Rev 36:2–24. https://doi.org/10.1016/j.oregeorev.2009.05.001
Hou ZQ, Yang ZM, Lu YJ, Kemp A, Zheng YC, Li QY, Tang JX, Yang ZS, Duan LF (2015) A genetic linkage between subduction- and collision-related porphyry Cu deposits in continental collision zones. Geology 43:247–250. https://doi.org/10.1130/G36362.1
Hou ZQ, Xu B, Zheng YC, Zheng HW, Zhang HR (2021) Mantle flow: The deep mechanism of large-scale growth in Tibetan Plateau. Sci Bull 66:2671–2690. https://doi.org/10.1360/TB-2020-0817
Jiang GZ, Gao P, Rao S, Zhang LY, Tang XY, Huang F, Zhao P, Pang ZH, He LJ, Hu SB, Wang JY (2016) Compilation of heat flow data in the continental area of China. Chin J Geophys Chin 59:2892–2910. https://doi.org/10.6038/cjg20160815
Kapp P, Taylor M, Stockli D, Ding L (2008) Development of active low-angle normal fault systems during orogenic collapse: insight from Tibet. Geology 36:7–10. https://doi.org/10.1130/G24054A.1
Kapp P, DeCelles PG (2019) Mesozoic-Cenozoic geological evolution of the Himalayan-Tibetan orogen and working tectonic hypotheses. Am J Sci 319:159–254. https://doi.org/10.2475/03.2019.01
Kelbert A, Meqbel N, Egbert GD, Tandon K (2014) ModEM: a modular system for inversion of electromagnetic geophysical data. Comput Geosci 66:40–53. https://doi.org/10.1016/j.cageo.2014.01.010
Liang XF, Chen Y, Tian XB, Chen YSJ, Ni J, Gallegos A, Klemperer SL, Wang ML, Xu T, Sun CQ, Si SK, Lan HQ, Teng JW (2016) 3D imaging of subducting and fragmenting Indian continental lithosphere beneath southern and central Tibet using body-wave finite-frequency tomography. Earth Planet Sc Lett 443:162–175. https://doi.org/10.1016/j.epsl.2016.03.029
Li JT, Song XD (2018) Tearing of Indian mantle lithosphere from high-resolution seismic images and its implications for lithosphere coupling in southern Tibet. Proc Natl Acad Sci U S A 115:8296–8300. https://doi.org/10.1073/pnas.1717258115
Molnar P, England P, Martinod J (1993) Mantle dynamics, uplift of the Tibetan Plateau, and the Indian Monsoon. Rev Geophys 31:357–396. https://doi.org/10.1029/93RG02030
Murphy MA, Saylor JE, Ding L (2009) Late Miocene topographic inversion in southwest Tibet based on integrated paleoelevation reconstructions and structural history. Earth Planet Sc Lett 282:1–9. https://doi.org/10.1016/j.epsl.2009.01.006
Pan GT, Wang LQ, Zhang WP, Wang BD (2013) Tectonic map and description of Qinghai-Tibet Plateau and its adjacent areas. Geological Publishing House, Beijing
Pang YJ, Zhang H, Gerya TV, Liao J, Cheng HH, Shi YL (2018) The mechanism and dynamics of N-S rifting in southern Tibet: insight from 3-D thermomechanical modeling. J Geophys Res-Solid Earth 123:859–877. https://doi.org/10.1002/2017JB014011
Rippe D, Unsworth M (2010) Quantifying crustal flow in Tibet with magnetotelluric data. Phys Earth Planet Inter 179:107–121. https://doi.org/10.1016/j.pepi.2010.01.009
Rodi W, Mackie RL (2001) Nonlinear conjugate gradients algorithm for 2-D magnetotelluric inversion. Geophysics 66:174–187. https://doi.org/10.1190/1.1444893
Rosenberg CL, Handy MR (2005) Experimental deformation of partially melted granite revisited: implications for the continental crust. J Metamorph Geol 23:19–28. https://doi.org/10.1111/j.1525-1314.2005.00555.x
Sheng Y, Jin S, Comeau MJ, Dong H, Zhang LT, Lei LL, Li BC, Wei WB, Ye GF, Lu ZW (2021) Lithospheric structure near the Northern Xainza-Dinggye rift, Tibetan Plateau-implications for rheology and tectonic dynamics. J Geophys Res-Solid Earth 126:e2020JB021442
Styron RH, Taylor MH, Murphy MA (2011) Oblique convergence, arc-parallel extension, and the role of strike-slip faulting in the High Himalaya. Geosphere 7:582–596. https://doi.org/10.1130/GES00606.1
Ten Grotenhuis SM, Drury MR, Spiers CJ, Peach CJ (2005) Melt distribution in olivine rocks based on electrical conductivity measurements. J Geophys Res-Solid Earth 110:B12201. https://doi.org/10.1029/2004JB003462
Unsworth MJ, Jones AG, Wei W, Marquis G, Gokarn SG, Spratt JE (2005) Crustal rheology of the Himalaya and Southern Tibet inferred from magnetotelluric data. Nature 438:78–81. https://doi.org/10.1038/nature04154
Wang G, Wei WB, Ye GF, Jin S, Jing JE, Zhang LT, Dong H, Xie CL, Omisore BO, Guo ZQ (2017) 3-D electrical structure across the Yadong-Gulu rift revealed by magnetotelluric data: new insights on the extension of the upper crust and the geometry of the underthrusting Indian lithospheric slab in southern Tibet. Earth Planet Sc Lett 474:172–179. https://doi.org/10.1016/j.epsl.2017.06.027
Wei WB, Jin S, Ye GF, Deng M, Jing JE, Unsworth M, Jones AG (2010) Conductivity structure and rheological property of lithosphere in Southern Tibet inferred from super-broadband magnetotelluric sounding. Sci China-Earth Sci 53:189–202. https://doi.org/10.1007/s11430-010-0001-7
Williams H, Turner S, Kelley S, Harris N (2001) Age and composition of dikes in southern Tibet: new constraints on the timing of east-west extension and its relationship to postcollisional volcanism. Geology 29:339–342. https://doi.org/10.1130/0091-7613(2001)029%3c0339:AACODI%3e2.0.CO;2
Ye GF, Unsworth M, Wei WB, Jin S, Liu ZL (2019) The lithospheric structure of the solonker suture zone and adjacent areas: crustal anisotropy revealed by a high-resolution magnetotelluric study. J Geophys Res-Solid Earth 124:1142–1163. https://doi.org/10.1029/2018JB015719
Yin A, Harrison TM (2000) Geologic evolution of the himalayan-tibetan orogen. Annu Rev Earth Planet Sci 28:211–280. https://doi.org/10.1146/annurev.earth.28.1.211
Yin A (2000) Mode of cenozoic east-west extension in Tibet suggesting a commonorigin of rifts in Asia during the Indo-Asian collision. J Geophys Res-Solid Earth 105:21745–21759. https://doi.org/10.1029/2000jb900168
Yin A (2006) Cenozoic tectonic evolution of the Himalayan orogen as constrained by along-strike variation of structural geometry, exhumation history, and foreland sedimentation. Earth-Sci Rev 76:1–131. https://doi.org/10.1016/j.earscirev.2005.05.004
Zhao ZD, Mo XX, Nomade S, Paul RR, Zhou S, Dong GC, Wang LL, Zhu DC, Liao ZL (2006) Post-collisional ultrapotassic rocks in Lhasa Block, Tibetan Plateau: Spatial and temporal distribution and it's implications. Acta Petrol Sin 22:787–794
Zhao JM, Yuan XH, Liu HB, Kumar P, Pei SP, Kind R, Zhang ZJ, Teng JW, Ding L, Gao X, Xu Q, Wang W (2010) The boundary between the Indian and Asian tectonic plates below Tibet. Proc Natl Acad Sci U S A 107:11229–11233. https://doi.org/10.1073/pnas.1001921107
Zheng YC, Hou ZQ, Fu Q, Zhu DC, Liang W, Xu PY (2016) Mantle inputs to Himalayan anatexis: insights from petrogenesis of the Miocene Langkazi leucogranite and its dioritic enclaves. Lithos 264:125–140. https://doi.org/10.1016/j.lithos.2016.08.019